THESIS FOR THE DEGREE OF DOCTOR OF PHILOSOPHY

Vertical-Cavity Surface-Emitting Lasers with Monolithically Integrated Metasurfaces

Erik Strandberg



CHALMERS

Photonics Laboratory
Department of Microtechnology and Nanoscience (MC2)
Chalmers University of Technology
Göteborg, Sweden, 2026

Vertical-Cavity Surface-Emitting Lasers with Monolithically Integrated Metasurfaces
Erik Strandberg

©Erik Strandberg, 2026

ISBN: 978-91-8103-477-6
Doktorsavhandlingar vid Chalmers tekniska högskola
Ny serie nr 5934
ISSN 0346-718X

Photonics Laboratory
Department of Microtechnology and Nanoscience (MC2)
Chalmers University of Technology
SE–412 96 Göteborg
Sweden
Telephone: +46 (0)31–772 10 00

Front cover illustration: An artistic drawing of a metasurface-integrated VCSEL with a metalens to collimate the emitted beam. The image was drawn by my friend and wonderful painter, Love Terins.
https://www.loveterins.com/

Printed in Sweden by
Reproservice
Chalmers Tekniska Högskola
Göteborg, Sweden, 2026

Vertical-Cavity Surface-Emitting Lasers with
Monolithically Integrated Metasurfaces

Erik Strandberg
Chalmers University of Technology, Department of Microtechnology
and Nanoscience, Photonics Laboratory

Abstract

The vertical-cavity surface-emitting laser (VCSEL) is a ubiquitous optoelectronic device, for example, powering short-reach communication in data centers and facial recognition. Its claim to fame is its small cavity, which enables low threshold currents, lasing within a single longitudinal mode, and excellent high-speed modulation. However, the small cavity size also implies a significant beam divergence, which means that the VCSEL is typically butt-coupled to a fiber, integrated with microlenses, or packaged with bulky external optics. The latest paradigm of miniaturized beam-shaping optics is called metasurfaces, nanostructures with a thickness similar to the wavelength of light and capable of imparting arbitrary phase profiles and polarization states to an incident beam. By integrating a metasurface directly in the substrate of the VCSEL, its compactness is preserved, thereby eliminating bulky optics and delivering an on-chip, tailored beam.

In this thesis, I present the design and fabrication of single-mode, single-polarization, bottom-emitting VCSELs monolithically integrated with GaAs metasurfaces. These devices are thereafter utilized for miniaturized biophotonic illumination modules. To overcome the aspect-ratio-dependent etching limits inherent to monolithic integration without an etch stop-layer, I demonstrate an unconventional metasurface design capable of shaping the VCSEL emission at exceptionally steep angles ($> 60°$) with high efficiency (> 90 %). These metasurface-integrated VCSELs enable the realization of a combined dark-field and total-internal-reflection microscopy module, alongside a surface plasmon resonance sensor with near state-of-the-art sensitivity, in a new integrable, flat format.

Keywords: vertical-cavity surface-emitting lasers, metasurfaces, metagratings, monolithic integration, miniaturized biophotonics, surface plasmon resonance

Sammanfattning

Den ytemitterande vertikala kavitetslasern (VCSEL:n) är idag en mycket vanlig optoelektronisk komponent som till exempel driver kortdistanskommunikation i datacenter och ansiktsigenkänning i din telefon. Dess framgång kommer från dess mikrokavitet, vilken möjliggör låga tröskelströmmar, emission i en enda longitudinell mod samt utmärkt höghastighetsmodulering. Men den lilla kaviteten medför också en betydande stråldivergens, vilket innebär att VCSEL:ar vanligtvis kopplas direkt till en optisk fiber eller paketeras med mikrolinser eller skrymmande extern optik. Det senaste paradigmet inom miniatyriserad strålformande optik kallas metaytor. Metaytor är nanostrukturer med en tjocklek i storleksordningen av ljusets våglängd, som kan tillföra en godtycklig fasprofil och polarisationstillstånd till en infallande stråle. Genom att integrera en metayta tillsammans med VCSEL:n så elimineras behovet av skrymmande optik och laserns kompakta format bevaras, samtidigt som en skräddarsydd ljusstråle kan levereras direkt från halvledarchippet.

I denna avhandling presenterar jag designen av och tillverkningsprocessen för bottenemitterande singel-mod VCSEL:ar med låst polarisation och monolitiskt integrerade GaAs-metaytor. Lasarna har möjliggjort realiseringen av miniatyriserade belysningsmoduler för biofotonik. Jag demonstrerar en okonventionell metaytedesign som kringgår de fundamentala begränsningarna i aspektrelationsberoende etsning vid monolitisk integrering utan etsstopp och kan deflektera ljuset från en VCSEL till mycket branta vinklar ($> 60°$), med exceptionellt hög effektivitet ($> 90\,\%$). Dessa VCSEL:ar möjliggjorde en mikroskopmodul för kombinerad mörkfälts- och total intern reflektionsmikroskopi samt en ytplasmonresonanssensor med en känslighet nära state-of-the-art-utrustning, men i ett nytt, integrerbart, miniatyriserat och platt format.

Transparency declaration

The thesis is written as a continuation of my earlier published licentiate thesis[1]. The writing of the thesis has been assisted by an AI-powered spell checker. No generative AI tools were used to generate scientific content, perform analysis, or formulate conclusions, and the author takes full responsibility for the contents of the thesis.

Erik Strandberg, August 2026

[1] Erik Strandberg, *Vertical-Cavity Surface-Emitting Lasers with Facet-Etched Metasurfaces*, Chalmers Tekniska Högskola 2024, ISSN 1652-0769.

Publications

This thesis is based on the work contained in the following papers:

[A] Mindaugas Juodėnas, **Erik Strandberg**, Alexander Grabowski, Johan Gustavsson, Hana Jungová-Šipová, and Mikael Käll,
"High-angle deflection of metagrating-integrated laser emission for high-contrast microscopy",
Light: Science and Applications, vol. 12, no. 1, p. 251, 2023

[B] **Erik Strandberg**, Mindaugas Juodėnas, Hana Jungová-Šipová, and Mikael Käll,
"Flat Plasmonic Biosensor with an On-Chip Metagrating-Integrated Laser",
ACS: Sensors, vol. 10, no. 10, pp. 7670–7678, 2025

[C] **Erik Strandberg**, Mindaugas Juodėnas, Alexander Grabowski, Åsa Haglund, and Anders Larsson,
"Buried subwavelength gratings for polarization pinning of bottom-emitting GaAs VCSELs",
IEEE: Selected Topics on Quantum Electronics, vol. 32, no. 6, pp. 1701408–1701408, 2026.

Related publications not included in the thesis:

[D] Doğukan Apaydın, Hjalmar Andersson, Lukas Uhlig, Sarina Graupeter, Joachim Ciers, Giulia Cardinali, **Erik Strandberg**, Tim Wernicke, Michael Kneissl, Ulrich Theodor Schwarz, Philippe Tassin and Åsa Haglund,
"Deep-UV Photonic Crystal Surface-Emitting Lasers",
Laser & Photonics Reviews, vol. 20, no. 6, p. e00271, 2026

Related conference contributions not included in the thesis:

[E] **Erik Strandberg**, Mindaugas Juodėnas, Alexander Grabowski, Johan Gustavsson, Hana Jungová-Šipová, and Mikael Käll, "Curved metagrating monolithically integrated with a vertical-cavity surface-emitting laser for efficient oblique emission", *SPIE: High Contrast Metastructures XIII*, San Francisco, USA 2024.

[F] Mindaugas Juodėnas, **Erik Strandberg**, Alexander Grabowski, Johan Gustavsson, Hana Jungová-Šipová, and Mikael Käll, "Miniature photonics devices enabled by metagrating-integrated VCSELs", *SPIE: Metamaterials XIV*, Strasbourg, France, 2024.

[G] Mindaugas Juodėnas, **Erik Strandberg**, Alexander Grabowski, Johan Gustavsson, Hana Jungová-Šipová, and Mikael Käll, "Strongly deflecting metagratings integrated on lasers for biophotonics", *Functional materials and nanotechnologies + Nanotechnology and innovation in the Baltic Sea regions*, Tartu, Estonia, 2024.

[H] **Erik Strandberg**, Mindaugas Juodėnas, Hana Jungová-Šipová, and Mikael Käll, "Enabling flat and miniaturized surface plasmon biosensing with metagrating-integrated lasers", *SPIE: Optical Sensors*, Prague, Czech Republic, 2025.

[I] Oliver Olsson, Khosro Zangeneh Kamali, **Erik Strandberg**, Hana Jungová-Šipová, and Mikael Käll, "On-Chip Lasers on Waveguides: A Meta-Morphosis in Waveguide Imaging!", *International Conference on Metamaterials, Photonic Crystals and Plasmonics*, Malaga, Spain 2025.

[J] Khosro Zangeneh Kamali, Oliver Olsson,**Erik Strandberg**, Hana Jungová-Šipová, and Mikael Käll, "On-chip angle-scanning scattering microscopy with all-dielectric metasurfaces and surface-emitting lasers", *International Conference on Metamaterials, Photonic Crystals and*

Plasmonics, Malaga, Spain 2025.

[K] **Erik Strandberg**, Mindaugas Juodėnas, Alexander Grabowski, Åsa Haglund, and Anders Larsson
"Deeply-etched Subwavelength Gratings for Polarization Pinning of Bottom-Emitting Vertical-Cavity Surface-Emitting Lasers",
Compound Semiconductor Week, Banff, Canada, 2025.

[L] Khosro Zangeneh Kamali, Oliver Olsson,**Erik Strandberg**, Hana Jungová-Šipová, and Mikael Käll,
"Integrated VCSEL–metasurface platform for on-chip imaging and sensing",
SPIE: Optical and Photonic Microsystems: Technology and Applications, Strasbourg, France, 2026.

Contents

Abstract **iii**

Sammanfattning **v**

Publications **ix**

Acknowledgement **xv**

Acronyms **xvii**

1 Introduction **1**
1.1 Background 1
1.2 Motivation for this work 9
1.3 State of the art 9
1.4 Thesis outline 10

2 VCSELs **13**
2.1 Laser fundamentals 13
2.2 Components of the VCSEL 17
2.2.1 Gain medium and quantum wells 17
2.2.2 Distributed Bragg reflectors 19
2.2.3 Longitudinal modes 21
2.2.4 Oxide aperture 23
2.2.5 Polarization state 26
2.3 VCSEL fabrication 31
2.4 Static VCSEL characterization 34

3 High-contrast dielectric metasurfaces **39**
3.1 Beam shaping with dielectric metasurfaces 40
3.2 Phase mapped metasurface 43

3.2.1 Dynamic phase metasurfaces 45
3.2.2 Resonant phase metasurface 47
3.2.3 Geometric phase metasurfaces 48
3.2.4 Arbitrary polarization metasurfaces 51
3.3 Beam shaping with superunit cell metasurfaces 55
3.3.1 Phase profile for the superunit cell metasurfaces . . 58
3.4 Metasurface simulations 61
3.4.1 Individual metaatoms with periodic boundaries . . 61
3.4.2 Superunit cell simulations 64
3.4.3 Metaatom simulation with FEM 65
3.5 Metasurface fabrication 67
3.5.1 Process flow for GaAs metasurfaces 67
3.5.2 Aspect-ratio dependent etching 69
3.6 Transmission characterization of metasurfaces 70
3.6.1 Stokes parameters 73
3.6.2 Fabricated metasurfaces 75

4 VCSELs with monolithically integrated metasurfaces 79
4.1 Dynamic-phase MS-VCSELs 79
4.2 Geometric-phase MS-VCSELs 82
4.3 Arbitrary polarization metasurface MS-VCSELs 84
4.4 Offset-axicon MS-VCSELs 87

5 Miniature integrated biophotonics 89
5.1 Miniaturized biophotonics with MS-VCSELs 89
5.2 Dark-field and total internal reflection microscopy 91
5.3 Surface plasmon resonance 93
5.4 Optical tweezing 96

6 Future outlook 101

7 Summary of Papers 103

Included papers A–C 129

Acknowledgement

First and foremost, I would like to extend my biggest possible thank you to Åsa, both for introducing me to the photonics lab and to VCSELs, and for support, guidance, and encouragement over the last five years. Thank you, Mikael, for inviting me to the bio-nanophotonics floor and for the general excitement about photonics and optics. Thank you, Anders, for a smooth introduction to the Ph.D. journey and the cleanroom duties, and Philippe, for support from the physics department and the cluster time for the students.

Beyond the professors, a very special thank you to Mindaugas for your nanofabrication expertise and for making the bioimaging lab thoroughly enjoyable to work in. I will not dwell too long on what I would have done without you, and I am hopeful to be able to pet a goat at your house soon. Alexander, my cleanroom guru, thank you for the introduction to chess and a steady stream of internet content. Thank you, Oliver, for keeping on figuring out what is actually going on with the MS-VCSELs and really looking forward to seeing some nano diamond-sensing, and thank you, Hana, for the orientation in biophotonics and on pipettes. To the other final VCSEL Ph.D. student in the optoelectronic lab, Hans, thank you for all the spare snus and your ability to even make the tropical heat of Shenzhen enjoyable. Thank you to Lars for all the discussions about how optics actually work and, of course, the chess swashbuckling. Thank you, Timo, for making my last thesis-writing session during COVID smell of menthol instead of just being lonely, and thank you to Johan for the latest and greatest thesis writing session. Thank you to Yan, my office neighbor of almost five years, I am certain that you will resolve the mystery of the scientific journal in Hong Kong. And thank you to my new office neighbor, Mia, I am looking forward to seeing where the Ph.D. journey takes you. Emilie, thank you for bringing laughs and positive energy to the sixth floor, and thank you, Niclas, for all the electron-beam

lithography support and the unprecedented amount of joy you bring to nanofabrication. Phuc, for raising not only my morale but the entire photonics floor, I am patiently looking forward to your next 3d models. I had the great pleasure of guiding a handful of student projects in the optoelectronic lab: Isac, Christoffer, Sofia, Jacob, Theodor, and Gustav. Thank you, and I wish you all the best in your future endeavors. And a special student thank you to Tintin for some intense nanofabrication. Of course, a huge thank you to everyone else from the photonics lab, bio-nanophotonics department, and the myfab cleanroom. Thank you to Simon, Per, Frida, and Erika for making the first five years of the physics education thoroughly enjoyable. Thank you to Love and Einar, Love for the beautiful artwork and Einar for the introduction to the god-fearing Bob, looking forward to taking the night train to Umeå. A thank you to my oldest friends, Gabriel, Pontus, Arvid, Björn, if you want to move in together again, I am interested. Thank you to the members of Ringöns most promising up-and-coming band, *Tack Så Mycket*, Viktor, Karl, and Roberto, for some well-needed Thursday respite. Thank you to my Alingsås family, father Gustav, Karin, Tulla, Olle, and Ellen, for taking me away from the city and getting my nose up from the keyboard. And thank you to my Linköping family, David and Fatima, for all the video games and tacopie. To my mother Sophia, thank you for every successful caravan trip and holiday celebration, I wish for several more in the coming years. The final thank you is reserved for the coolest cat in your town, Hanna. I really, really like her.

Erik Strandberg
Göteborg, Sweden
31 August 2026

Acronyms

AlAs	Aluminum Arsenide
AlGaAs	Aluminum Gallium Arsenide
APM	Arbitrary Polarization Metasurface
AR	Anti-Reflection
ARDE	Aspect-Ratio-Dependent Etching
CCD	Charge-Coupled Device
DBR	Distributed Bragg Reflector
DF	Dark-Field
EBL	Electron Beam Lithography
EEL	Edge-Emitting Laser
FEM	Finite Element Method
FSR	Free Spectral Range
GaAs	Gallium Arsenide
HF	Hydrofluoric Acid
HMDS	Hexamethyldisilazane
ICP	Inductively Coupled Plasma
InGaAs	Indium Gallium Arsenide
IPA	Isopropyl Alcohol
IPV	Current-Power-Voltage measurement
LASER	Light Amplification by Stimulated Emission of Radiation
LCP	Left-Hand Circular Polarization
LED	Light-Emitting Diode
LP	Linearly Polarized
MOCVD	Metal-Organic Chemical Vapor Deposition
MQW	Multiple Quantum Well
MS-VCSEL	Metasurface-Integrated Vertical-Cavity Surface-Emitting Laser
NA	Numerical Aperture
OPSR	Orthogonal Polarization Suppression Ratio
OSA	Optical Spectrum Analyzer

PB	Pancharatnam-Berry
PD	Photodiode
PDMS	Polydimethylsiloxane
PIP	Polarization-Resolved Current-Power measurement
QW	Quantum Well
QWP	Quarter-Waveplate
RCP	Right-Hand Circular Polarization
RIE	Reactive Ion Etch
RIE-ICP	Reactive Ion Etch-Inductively Coupled Plasma
RIU	Refractive Index Unit
SEM	Scanning Electron Microscope
SMSR	Side-Mode Suppression Ratio
SPP	Surface Plasmon Polariton
SPR	Surface Plasmon Resonance
TIR	Total Internal Reflection
TLM	Transfer Length Method
TMM	Transfer Matrix Method
VCSEL	Vertical-Cavity Surface-Emitting Laser

Chapter 1

Introduction

1.1 Background

The term *laser* is an acronym for **L**ight **A**mplification by **S**timulated **E**mission of **R**adiation. The possibility of generating light via *stimulated emission* was mathematically formulated by Einstein as early as 1916. He mathematically deduced the stimulated emission process, in which an incident photon can trigger an excited state in a medium to produce a second, identical photon. Although the mechanism was theoretically known, its first practical demonstration came forty years later, in 1955, when the *maser* achieved stimulated emission in the microwave regime ($\lambda = 1.25\,\text{cm}$) [1]. Translating this principle to the optical regime required another five years, a milestone achieved in 1960 with the demonstration of the first ruby laser [2]. Since then, the laser has arguably become one of the most transformative instruments across the natural sciences and throughout modern society. A laser is named after the material that constitutes its gain medium, the medium that can be pumped to generate optical gain via stimulated emission. With high likelihood, you have encountered a helium-neon (He-Ne) *gas* laser in an undergraduate lab session or an optics lecture. In the He-Ne gas laser, He atoms are kinetically excited by an electrical discharge, which thereafter excites the electronic states of the Ne atoms through collisions. The desired stimulated emission occurs as the Ne atoms transition from the $3s \rightarrow 2p$ electron energy states, producing a clear red beam at $\lambda = 632.8$ nm [3].

Semiconductor lasers utilize the direct bandgap of a semiconductor

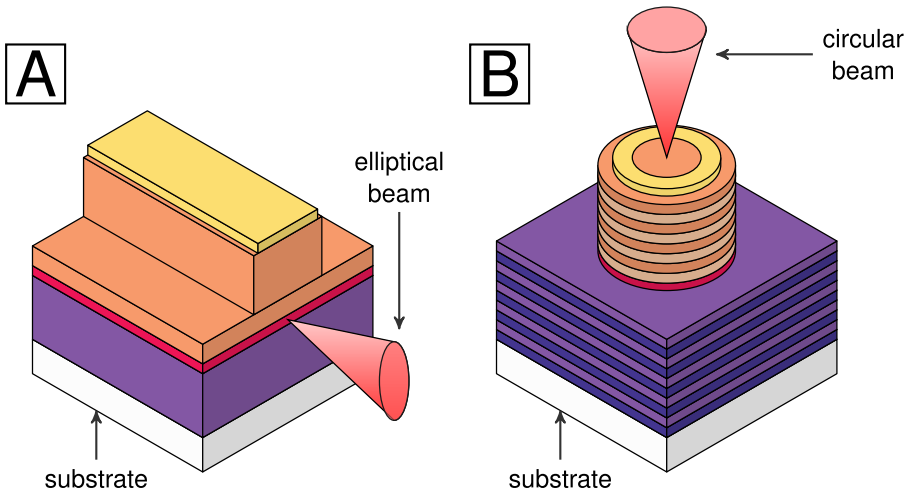

Figure 1.1: **A)** Schematic view of an edge-emitting laser (EEL) with elliptical emission from the cleaved facet. **B)** Schematic view of a vertical-cavity surface-emitting laser (VCSEL) emitting a circularly symmetric beam propagating normal to the substrate surface.

to generate stimulated emission [4] and are today ubiquitous devices. Because they can be manufactured using micro- and nanofabrication techniques, they can be produced in large, wafer-scale quantities, yielding small and affordable emitters. Although they typically have lower absolute power output than, for example, gas or solid-state lasers, they offer other performance advantages beyond their small size. Most notably, semiconductor lasers offer high-speed modulation capabilities [5], high optical power conversion efficiencies [6, 7], and low cost [8]. Additionally, the development (and success) of the transistor has driven considerable investments and advances in micro- and nanofabrication techniques over the past four decades [9]. In parallel, this has driven the advancement of semiconductor lasers, as they have benefited from the proliferation of new advanced fabrication technologies, increasingly lower-defect substrates, and refined epitaxial crystal-growth techniques [10].

The two primary types of semiconductor lasers are edge-emitting lasers (EELs) and vertical-cavity surface-emitting lasers (VCSELs) [11], as depicted in **Fig. 1.1**. As their names suggest, the main distinction lies in the emission direction relative to the wafer substrate. The EEL has

the optical cavity oriented along the substrate and emits light from the cleaved edges of the laser [12]. This geometry implies that the EEL has a longitudinal standing wave along the length of the gain medium, allowing a large overlap with the lasing mode, which can thus acquire a large amount of optical gain per round trip in the cavity. This large gain implies that the cavity mirrors can sustain lasing with relatively low reflectance. Often, the edge is simply cleaved, and the reflection from the refractive-index contrast between the high refractive index of the semiconductor and air is sufficient to act as a mirror ($R \approx 30\%$). However, the long cavity dictates that the EEL inherently supports lasing in several longitudinal modes, broadening the emission spectrum and distorting the emission profile. Furthermore, the emitted beam from the cleaved edge of the EEL usually has an elliptical shape. In contrast, the longitudinal standing wave in a VCSEL is perpendicular to the gain medium. This implies that the longitudinal overlap between the mode and the gain medium is much smaller, resulting in a tiny amount of gain per round trip. This requires the VCSEL mirrors to have exceptionally high reflectances ($R > 99\%$). However, the short cavity of the VCSEL comes with several advantages: a low lasing threshold [13, 14], inherent single-longitudinal-mode emission, and excellent high-speed modulation capabilities at low currents [15, 16]. In addition, the VCSEL can be fabricated with a circular aperture, generating a circularly shaped beam suitable for coupling light into a fiber, and its vertical geometry also allows VCSELs to be fabricated in dense two-dimensional arrays [17] and tested on-wafer for electrical and optical screening during fabrication.

Since the conceptual inception of the VCSEL in 1979 [18] and its subsequent commercialization in 1996 [19], the infrared-emitting gallium arsenide (GaAs) VCSEL has found widespread use in short-reach optical communications and sensing. Although GaAs VCSEL technology is highly mature, continuous improvements are still being discovered. For example, researchers utilize photon–photon resonances in bow-tie-shaped cavities [20], shape emission apertures for speckle-free illumination [21, 22], integrate multiple tunnel junctions for higher power conversion efficiencies [23], and incorporate etched grating-relief arrays into the VCSEL cap [24]. Today, the GaAs VCSEL is firmly established as the light source for short-reach fiber-optic data links in data centers [25, 26]. Beyond communications, VCSELs have seen extensive use for sensing, with early applications in optical computer

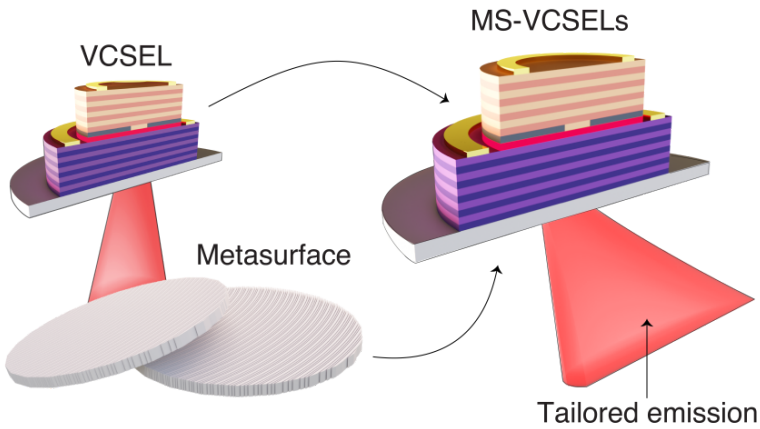

Figure 1.2: The central component of this thesis: the metasurface-integrated vertical-cavity surface-emitting laser (MS-VCSEL). By etching a metasurface in the substrate of a bottom-emitting VCSEL, the emitted beam can be tailored directly from the semiconductor chip.

mice [27] and more modern applications, such as optical excitation of rubidium for atomic clocks [28] and miniature solid-state gyroscopes [29]. Furthermore, the ability to densely pack VCSELs into two-dimensional arrays has enabled their use in laser printing [30], smartphone facial recognition systems [31], high-resolution time-of-flight cameras, augmented and virtual reality headsets [32,33], and high-power VCSEL arrays for solid-state light detection and ranging systems [34]. However, the microscopic cavity of the VCSEL means that the emitted beam typically exhibits significant divergence. Therefore, the VCSEL is usually butt-coupled to an optical fiber, packaged with microlenses, or requires bulky external optics to shape the emitted beam. Whether the VCSEL is intended for laboratory use or as an integrated source within a larger device, these solutions limit the final device size or the emission profiles that can be generated.

One of the most impactful recent developments in nanophotonics is metamaterials [35, 36], which are artificially structured media composed of subwavelength constituents [37], referred to as metaatoms, enabling extraordinary manipulation of electromagnetic waves [38, 39]. A metasurface is the two-dimensional version of a metamaterial, where a material is patterned with a flat lattice of subwavelength metaatoms to achieve a specific optical response [40]. In principle, the metasurface

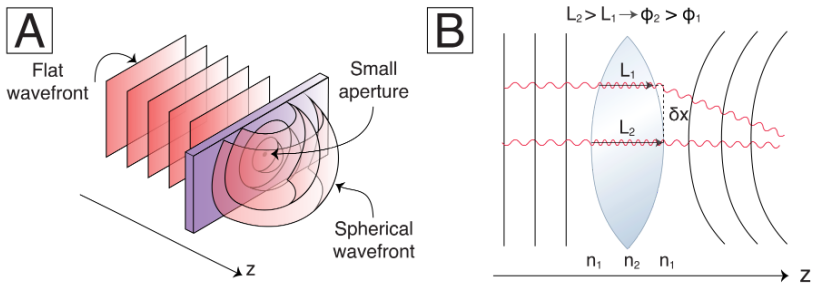

Figure 1.3: A) A plane wave propagating through a small aperture, producing a diverging spherical wavefront. **B)** The higher refractive index glass (n_2) compared to the surrounding air (n_1) creates a transversely dependent (δx) phase shift due to the glass geometry.

can replicate (and in some cases outperform) classical refractive optical components [41, 42]. However, the major advantage of a metasurface is that it achieves this within an optical component that has a thickness on the order of the wavelength ($\approx$ hundreds of nm) [43]. By integrating the metasurface together with a bottom-emitting VCSEL, its small size can be fully utilized, producing a tailored beam shape directly on-chip. This component, called a metasurface-integrated vertical-cavity surface-emitting laser (MS-VCSEL), is the central component of this thesis. In **Fig. 1.2**, a bottom-emitting VCSEL is illustrated emitting a divergent Gaussian beam downwards through the substrate. By integrating a metasurface into the laser substrate, external optics can be eliminated.

The shape of a beam is determined by its wavefront, i.e., surfaces of constant phase in the field, and wave propagation is typically illustrated by drawing lines that mark the wavefront. This is exemplified in **Fig. 1.3A**, which illustrates a plane wave propagating through an aperture. The incident plane wave has a uniform phase profile, or a flat wavefront, which implies that the entire wave propagates in the same direction. When it encounters the small aperture, the wave diffracts, transforming the wavefront into a spherical front and causing the wave to spread out. While shaping the wavefronts of light with shaped glass, a refractive optical component, has long been known, research has continued to shrink and unlock new functionalities for different beam-shaping components. In this pursuit, the flat metasurface represents the

latest paradigm in miniaturized, advanced beam shaping. A classical refractive optical element, such as a glass lens, shapes the wavefront via the geometry of a medium with a higher refractive index (n_2) relative to the surrounding medium (n_1). Since light has a shorter effective wavelength within the higher refractive index medium, it accumulates phase faster per unit length, as schematically shown in **Fig. 1.3B**. The portion of a wave that propagates through a thicker section (L_2) of the lens thus acquires a larger phase delay ($\phi_2 > \phi_1$) compared to the wave propagating through a thinner section (L_1). This transversely varying phase delay, governed by the geometry, determines the new wavefront and thus shapes the beam.

The progression of miniaturizing beam-shaping optics is illustrated in **Fig. 1.4**, where the first step came with the realization that light is an electromagnetic wave. Since a wave is periodic, the accumulation of a phase shift of 2π shifts the wave by one full wavelength, simply returning the wave to its initial state. Therefore, to shape a beam, it is sufficient to shift the phase over the range 0–2π, which is referred to as full phase coverage. This realization led to the invention of the Fresnel lens[1], where redundant bulk glass that only contributes integer multiples of 2π to the phase accumulation is removed. As such, the stepped Fresnel lens can be much thinner while still imparting the same phase profile as the classic lens [44]. The next major step in miniaturization was the development of diffractive optics, a component enabled by modern nanofabrication techniques capable of structuring materials with dimensions comparable to the wavelength of light [45–47]. For the diffractive optical element, the varying phase delay similarly relies on phase accumulation as light propagates through a high-index medium. However, rather than utilizing a continuously varying geometry, the desired phase profile is discretized and etched into the material as a stepped pattern with varying heights. While diffractive optics can achieve complex beam manipulation [48], the technology poses a significant fabrication challenge because subwavelength features must be etched to several discrete depths with high precision.

The progression culminates with the high-contrast dielectric meta-

[1]Many lighthouses still utilize a Fresnel lens to shape the light from the beacon. If you are passing through southern Sweden, a visit to Kullen Lighthouse in Höganäs is highly recommended.

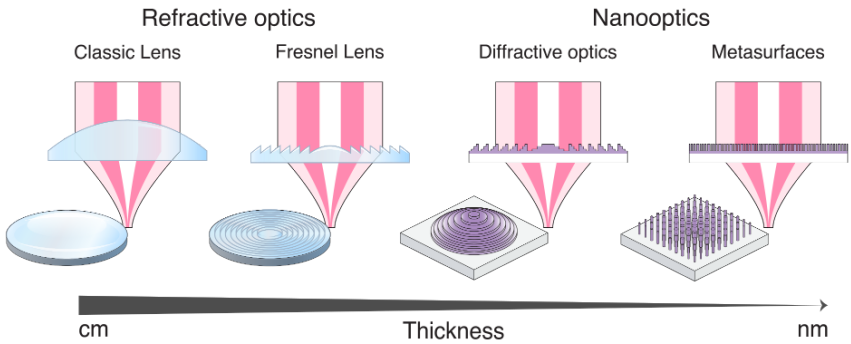

Figure 1.4: The progression of miniaturizing optical beam-shaping components, culminating in the high-contrast dielectric metasurface.

surface. Although they can be thought of in the same manner as diffractive optical elements, imparting a discretized phase profile, they no longer rely on phase accumulation through propagation in a bulk medium. Instead of varying the material thickness to achieve the necessary phase delay, the metasurface uses variations in the geometry of discrete nanoscatterers, called metaatoms, arranged in a two-dimensional subwavelength lattice [49, 50]. As schematically illustrated in **Fig. 1.5A**, the same modulation of the phase profile can now be achieved by designing the local phase delay ($\delta\phi_1$ and $\delta\phi_2$) of the scattering from the subwavelength metaatoms. The major fabrication advantage compared to diffractive optical elements is that the entire metasurface can be defined in a single lithographic step. In **Fig. 1.5B**, a scanning electron microscope (SEM) image of a fabricated GaAs metasurface is shown, which has the same functionality as a glass lens. The inset shows a zoomed-in SEM image of the metasurface edge, where the subwavelength metaatoms are visible. The varied geometry of the metaatoms determines the wavefront of a beam transmitted through the metasurface. In addition, a metasurface can use birefringent metaatoms to simultaneously modulate the polarization state and the desired phase profile [51, 52]. Metasurfaces [40] can effectively replicate the optical functionality of essentially any classical refractive or diffractive element, such as lenses [53, 54] and blazed gratings [55], while integrating advanced features like polarization conversion [56] or multiplexed combinations of all mentioned examples [57]. Remarkably, all of this optical functionality fits inside a single component with a physical thickness on the order of a wavelength.

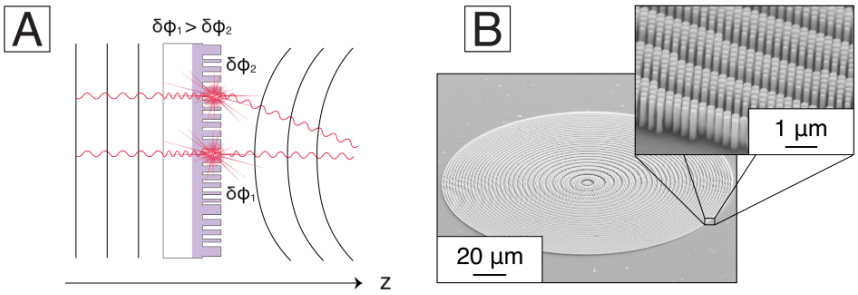

Figure 1.5: A) The geometry of individual metaatoms creates two different local phase delays ($\delta\phi_1$ and $\delta\phi_2$). By designing the geometry of these metaatoms, it is, for example, possible to replicate the phase profile created by the refractive lens in **Fig. 1.3**. **B)** SEM images of a fabricated GaAs metasurface. The metasurface in the image functions exactly like a refractive lens, but has a thickness of 700 nm, roughly 100 times thinner than the width of a human hair.

Despite the above-mentioned advantages, the operational bandwidth of metaatoms is limited because they fundamentally rely on resonances, unlike classical refractive optics. Developing broadband, highly efficient metasurfaces remains an ongoing challenge for metasurfaces to compete as an alternative to refractive optics [58]. Beyond the constraints of narrowband operation, metasurface fabrication today mainly relies on electron-beam lithography (EBL) to pattern subwavelength metaatoms. While EBL systems offer very good fidelity, they suffer from low throughput and are notoriously expensive. To address this, scalable, high-volume alternatives are steadily emerging, including nanoimprint lithography and self-assembled metasurfaces [59, 60]. In addition, metasurfaces can be integrated with active materials, paving the way for ultra-thin, dynamically reconfigurable optical beam shaping. Promising platforms include electrically tunable transparent indium tin oxide [61], thermally sensitive silicon structures [62], and liquid-crystal infiltration within resonant cavities [63].

1.2 Motivation for this work

The emitted light from a VCSEL is typically shaped by microlenses, bulky external beam-shaping optics, or butt-coupled optical fibers. These solutions are either limited in the different wavefronts they can create or constrain the overall size of the final device. By monolithically integrating a metasurface directly onto the substrate of a bottom-emitting VCSEL, we can preserve its small size while enabling arbitrary beam shaping directly from the chip. The GaAs VCSEL is an ideal candidate for monolithic integration with high-contrast dielectric metasurfaces. Because the VCSEL and the metasurface share compatible planar fabrication flows, the bottom-emitting VCSEL can be processed on one side of the wafer and then flipped to pattern the metasurface directly onto the outcoupling facet on the substrate side. Furthermore, the pristine, epitaxially grown GaAs substrate is well suited for metasurface fabrication, featuring a high refractive index and low defect density. In addition, a VCSEL inherently lases in a single longitudinal mode and, with careful processing, can be made to lase in a single transverse mode with a fixed linear polarization state. This yields a narrowband beam with a well-behaved Gaussian wavefront, matching the narrowband operational range of metasurfaces and providing a well-defined phase profile for metasurface design.

1.3 State of the art

The integration of optical metasurfaces with semiconductor lasers has advanced significantly in recent years [64, 65]. The earliest demonstrations of generating specialized wavefronts, such as orbital angular momentum, were achieved by patterning SiN_x metasurfaces directly onto VCSEL facets [66] or utilizing half-cavity configurations [67]. The first demonstration of a monolithic MS-VCSEL emerged in 2020, with the integration of dynamic-phase metasurfaces to collimate, deflect, and generate Bessel beams directly on-chip [68]. The same group has since applied their methodology to demonstrate highly complex array beams and holographic projections [69–72]. Furthermore, they also used so-called spin-decoupled metasurfaces, metasurfaces that combine both dynamic and geometric phase manipulation, enabling the projection of holographic images and vortex beams with different polarization

states from a single device [73–76]. Most recently, VCSELs have been developed with monolithically integrated beam-shaping metalenses to increase coupling efficiency to fibers for bottom-emitting high-speed VCSELs [77]. Beyond wavefront manipulation, metasurfaces have also been integrated within the VCSEL cavity itself. Amorphous silicon metasurfaces have been used to generate circularly polarized emission and, under reverse bias, to function as circular polarization-sensitive photodetectors [78]. GaAs metasurfaces have been embedded directly within the top distributed Bragg reflector (DBR) to simultaneously provide the requisite cavity reflectance while converting linear emission into circular polarization [79].

While these state-of-the-art demonstrations showcase the potential for arbitrary, on-chip beam shaping and holography with the MS-VCSEL, most remain isolated proof-of-concept demonstrations. This highlights the need to transition the light source beyond free-space projection and deploy it as a functional, scalable, and miniaturized module for specific applications.

1.4 Thesis outline

Chapter 2 describes the fundamental lasing action of a semiconductor laser, along with the design and fabrication of a bottom-emitting GaAs VCSEL for single-longitudinal and single-transverse mode emission, incorporating a subwavelength grating to pin the inherently unpredictable polarization state of a GaAs VCSEL (Paper **C**).

Chapter 3 introduces the principles of both conventional phase-mapped metasurfaces and superunit-cell metasurfaces. It details the methodologies for designing these structures and the processing steps required to fabricate high-contrast dielectric metasurfaces in GaAs.

Chapter 4 combines the discussion from the two previous chapters and presents the emission characteristics of the fabricated MS-VCSEL. It also outlines the limitations encountered with this type of monolithic integration for the MS-VCSEL.

Chapter 5 discusses the practical deployment of these integrated devices for miniaturized biophotonics. It introduces the theoretical

framework and experimental results for both the combined dark-field and total internal reflection microscopy module (Paper **A**) and the integrable surface plasmon sensor (Paper **B**).

Chapter 6 provides a brief summary and a future outlook on the scalability and applications of the MS-VCSEL.

Chapter 2

VCSELs

The vertical-cavity surface-emitting laser (VCSEL) is a semiconductor laser, most commonly fabricated by sandwiching a gain medium between two highly reflective distributed Bragg reflectors (DBRs). This chapter outlines the basic principles of lasing and the core components of a laser, then translates them to the epitaxial structure of the VCSEL. Emphasis is placed on fabricating a VCSEL that emits in a single transverse mode and with a pinned, predictable polarization state. These properties are crucial, since the following metasurface design depends on both the phase profile and the polarization state of the incident beam. The chapter ends with the fabrication and characterization of the static performance needed for the following metasurface integration of the bottom-emitting VCSELs.

2.1 Laser fundamentals

Photons generated in a cavity via *stimulated emission* are identical in wavelength, phase, and propagation direction, resulting in a beam that is monochromatic, highly coherent, and collimated (the signature properties of a laser). To construct a laser, the goal is to create conditions in which stimulated emission is the dominant radiative process, which is called lasing. This requires three main components: a medium that can generate light via stimulated emission at a desired wavelength (gain medium), an energy-pumping mechanism to inject carriers into the gain medium (to achieve population inversion), and an optical feedback mechanism to achieve a high photon density at the desired wavelength (optical cavity).

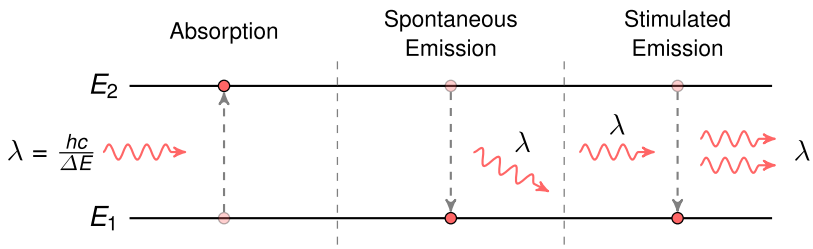

Figure 2.1: The discrete energy levels of the gain medium as a two-level system. In the two-level system, there are three possible electron-photon interactions: absorption, spontaneous emission, and stimulated emission. The coherent emission from a laser is linked to the generation of identical photons, in wavelength, phase, and direction, via the stimulated emission process.

Since the core mechanism, stimulated emission, is a quantum-mechanical process, it is instructive to study the two-level system[1], as illustrated in **Fig. 2.1**. In the two-level system, electrons populate either a higher excited (E_2) or a lower ground (E_1) energy state, where electrons and photons can exchange energy via three interactions: *absorption*, *spontaneous emission*, and *stimulated emission*, as depicted in **Fig. 2.1**. Spontaneous and stimulated emission are radiative processes because the energy from electron de-excitation is converted into a photon, generating light. The emitted photon has a wavelength that matches the energy difference between the two states

$$\lambda = \frac{hc}{\Delta E}. \tag{2.1}$$

Since photons in both radiative processes are generated by the de-excitation of carriers from the higher-energy state, the processes depend on the electron population in the excited state (N_2). This means that achieving net optical gain requires actively injecting energy into the gain medium. By injecting energy, a non-equilibrium state called population inversion can be established, in which the electron population in the excited state (N_2) exceeds that in the lower state (N_1), as illustrated in **Fig. 2.2A**. Energy injection is typically done by either supplying the gain medium with an electric current (electrical injection) or by

[1] In reality, lasing is not possible within just a two-level system due to saturation, but it provides a very clear model for explanation of the lasing action. For a deeper dive into lasing in the semiconductor laser, *Diode Lasers and Photonic Integrated Circuits* by Coldren is highly recommended [4].

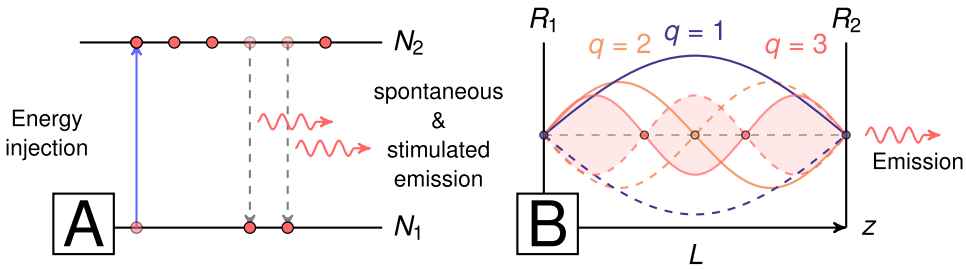

Figure 2.2: A) Population inversion ($N_2 > N_1$): Injection of energy into the gain medium excites electrons from the lower energy state (E_1) to the higher state (E_2), which increases the rate of spontaneous and stimulated emission. **B)** The optical cavity: A Fabry-Perot cavity creates standing waves in the electric field when half the wavelength is an integer (q) multiple of the optical length of the cavity (Ln_{eff}).

illuminating it with an external light source to excite electrons via absorption (optical injection).

Once population inversion ($N_2 > N_1$) is established, the gain medium actively generates light via both radiative processes, spontaneous and stimulated. The spontaneous emission, however, is an inherently random process driven by quantum vacuum fluctuations [4]. Because excited electrons decay stochastically, the generated photons lack a well-defined phase relationship and directionality, resulting in incoherent, isotropic emission[2]. Because stimulated emission is instead induced by a photon, the generated photons have the same phase and direction, creating highly coherent and directional emission. Furthermore, because the interaction is driven by photons, the rate is dependent on the photon density within the gain medium. Consequently, if the photon density (the electromagnetic field intensity) is sufficiently amplified, stimulated emission can become the dominant process, and lasing is achieved.

The amplification of the photon density is made possible by enclosing the gain medium within an optical cavity. The threshold for lasing is reached when the optical gain for one complete round trip precisely balances the total optical losses of the cavity. Once this threshold is

[2]Despite the incoherence, spontaneous emission is essential. It initiates the lasing process by coupling the first seed photons into the lasing mode, and it is the process utilized for light-emitting diodes (LEDs).

surpassed, an optical avalanche effect begins, and as the photon density rapidly grows, an intense electromagnetic field builds up within the cavity at the resonant wavelength, which initiates lasing. In addition, the self-oscillating process means that virtually all carriers in the excited state are consumed by stimulated emission, clamping the carrier density of the gain medium at the threshold value. The coherent emission is extracted via one cavity mirror with an intentionally lower reflectance.

The threshold material gain (g_{th}), i.e., the required gain that must be supplied to the electric field by the gain medium to achieve lasing—can be derived analytically by propagating an electric field through one complete round trip in a Fabry-Perot cavity with two planar mirrors [4], as illustrated in **Fig. 2.2B**. A plane wave propagating along the longitudinal z-axis inside the cavity can be expressed as

$$\mathbf{E}(x, y, z) = \mathbf{E}_t(x, y) e^{ikz} e^{\frac{1}{2}\Gamma(g-\alpha)z}, \tag{2.2}$$

where $\mathbf{E}_t(x, y)$ is the transverse electric field profile, k is the propagation constant of the longitudinal mode in the cavity, g is the gain coefficient, and α is the absorption coefficient per unit length of the gain medium (with the factor of two since they are usually defined for the electric field intensity). The optical confinement factor, Γ, denotes the longitudinal overlap between the optical standing wave and the gain medium. The electric field forms a stationary state inside the cavity when it perfectly reproduces itself after propagating one full round-trip ($2L$) in the cavity:

$$\mathbf{E}(x, y, z) = \mathbf{E}(x, y, z + 2L) \quad \rightarrow \quad 1 = \underbrace{e^{2ikL}}_{\text{Phase}} \underbrace{\sqrt{R_1 R_2} e^{(\Gamma g - \alpha)L}}_{\text{Amplitude}}, \tag{2.3}$$

where R_1 and R_2 are the reflectivities of the respective mirrors for the Fabry-Perot cavity, as seen in **Fig. 2.2B**. This expression can be separated into two conditions: one for the phase and one for the amplitude. First, the phase dictates the wavelength that will create a standing wave between the mirrors of the cavity,

$$1 = e^{2ikL} \quad \rightarrow \quad \lambda_0 = \frac{2Ln_{\text{eff}}}{q}, \tag{2.4}$$

where q is the mode number. This expression means that a standing wave is formed when the wavelength is an integer (q) multiple of a half-wavelength of the effective optical length of the cavity. In **Fig. 2.2B**,

the first three standing waves are illustrated. Secondly, for the amplitude of the field to remain the same after one round-trip, the gain needs to balance the losses, which leads to the expression

$$1 = \sqrt{R_1 R_2} e^{\Gamma(g-\alpha)2L} \quad \rightarrow \quad g_{\text{th}} \triangleq g = \frac{1}{\Gamma}\left(\alpha + \frac{1}{2L}\ln\frac{1}{R_1 R_2}\right), \quad (2.5)$$

where g_{th} is the threshold material gain. These terms represent the total losses the optical mode experiences per round-trip, which the gain medium must overcome to initiate lasing. The first term (α) is the internal propagation loss within the gain medium, while the second term ($\frac{1}{2L}\ln\frac{1}{R_1 R_2}$) represents the distributed mirror loss. This highlights the distinction between an EEL and a VCSEL: because an EEL has a significantly longer cavity (L), the optical mode is significantly amplified per round-trip in the cavity, allowing EELs to operate with much lower mirror reflectances (R_1 and R_2) than those required for VCSELs with shorter cavities.

2.2 Components of the VCSEL

2.2.1 Gain medium and quantum wells

Semiconductor lasers, including VCSELs, utilize the direct bandgap of an intrinsic (undoped) semiconductor as a gain medium. The active region is sandwiched between wider-bandgap *p*- and *n*-doped layers to form a *pin* heterostructure [80, 81]. The heterostructure facilitates efficient carrier injection to establish the requisite population inversion while simultaneously creating a potential well that longitudinally confines the carriers within the gain medium. The semiconductor layers of the gain medium can be grown very thin, forming quantum wells (QWs). With a thickness on the order of, or smaller than, the de Broglie wavelength of the electrons in the crystal lattice[3] [83], the QW induces a one-dimensional spatial quantization of the electron wavefunction, introducing several highly beneficial properties for semiconductor lasers [84].

Most notable is the modified density of states in the QW compared to a bulk semiconductor, altering the carrier energy distributions and

[3] As a reference for the size, the de Broglie wavelength of the electron in GaAs is $\lambda_{\text{dB}} \approx 20$–$30$ nm [82]

narrowing the gain spectrum [85, 86]. This allows population inversion at the band edge to be achieved at significantly lower excess carrier densities. In addition, the reduced volume of the gain medium with a QW requires fewer carriers to reach population inversion, which effectively lowers the device threshold current, even with a corresponding reduction in the optical confinement factor (Γ). Additionally, because QWs are so thin, they can be grown with a significant amount of built-in strain, enabling strain engineering to further tailor the band structure of the gain medium [87].

While individual QWs provide exceptionally high peak material gain, there is a limit to the maximum amplification a single well can supply. As the injected carrier density increases, the material gain of a typical indium gallium arsenide (InGaAs) QW[4] saturates around 3000 to 4000 cm^{-1} [88]. Saturation occurs because the lowest-energy states within the conduction and valence bands become fully occupied. Injecting additional carriers beyond this point does not increase gain at the lasing wavelength. Instead, it populates higher-order subbands and increases non-radiative loss mechanisms, such as Auger recombination. Therefore, the gain medium commonly utilizes multiple quantum wells (MQWs) separated by higher-bandgap barriers. With MQWs, the total gain volume and overall optical confinement factor (Γ) increase, and the gain can be distributed across multiple wells. This allows each individual well to operate in a more efficient, unsaturated regime (providing a material gain of 1000 to 2000 cm^{-1}), while collectively providing a total amplification high enough to reach the threshold gain. However, there is a limit to how many QWs can be stacked within one gain medium, as the carrier distribution across multiple wells becomes increasingly inhomogeneous. A very recent development for VCSELs, however, is the possibility of cascading multiple MQW regions via tunnel junctions. This enables a single electron to recombine several times, drastically increasing the gain [23].

The wavelength range over which the gain medium provides amplification for the optical field is called the gain spectrum. The peak wavelength and spectral bandwidth of this spectrum are determined by the material stoichiometry and the thickness of the QWs. The accessible emission wavelengths are practically constrained by lattice matching between the

[4]The material for the QWs in the fabricated lasers.

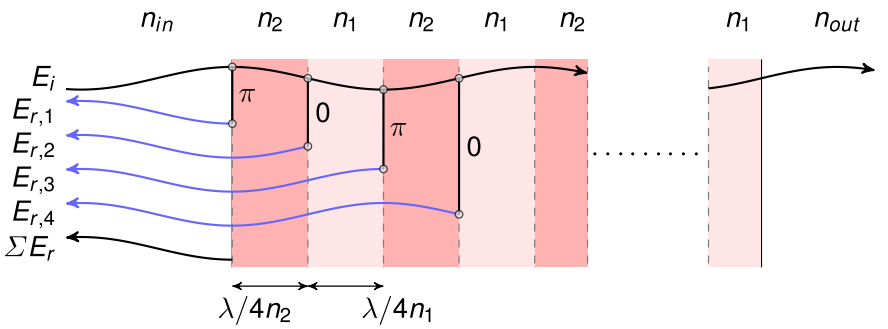

Figure 2.3: A schematic cross-section of the DBR, with the repeated layers of high- (n_2) and low- (n_1) refractive index with a quarter-wavelength optical thickness in either layer (λ_0/n). The figure shows the first four partial reflections for an incident wave (E_i).

gain medium, DBRs, and the underlying substrate. A GaAs substrate can support the epitaxial growth of VCSELs with emission spanning from deep-red ($\lambda = 660$–680 nm using InGaP QWs [89]) to near-infrared wavelengths ($\lambda = 1534$ nm using GaInNAsSb QWs [90]). Furthermore, at room temperature, the near-infrared gain spectrum of typical InGaAs used in the fabricated VCSELs can provide amplification over a bandwidth of 30 to 50 nm [84, 91].

2.2.2 Distributed Bragg reflectors

As seen from the mirror loss in **Eq. 2.5**, the combination of a very short cavity (L) and a small optical confinement factor (Γ) requires cavity mirrors (R_1 and R_2) with exceptionally high reflectances to support lasing. Because a VCSEL cavity length is typically a few wavelengths (1–10λ) with a typical optical confinement of 1–5%, the mirror reflectances must exceed 99%. This large reflectivity is necessary to keep the threshold material gain (g_{th}) in the achievable range for an MQW gain medium (1000–2000cm^{-1}). To realize such large reflectivities, the VCSEL cavity is most commonly formed with DBRs.

A DBR consists of alternating layers of high- (n_2) and low- (n_1) refractive-index media, each with a thickness of one-quarter of the wavelength in the respective medium ($\frac{\lambda_0}{4n}$). The principle is that the DBR creates constructive interference for all the partial reflections at the periodic interfaces. This can yield a very large reflectance within a certain wave-

length range (the DBR stopband), depending on the refractive-index contrast, the number of layers, and the thicknesses of the layers. A cross-section of the DBR is schematically illustrated in **Fig. 2.3**, where the first four first-order partial reflections are shown. When an incident wave (E_i) from air ($n_{\text{in}} = 1$) propagates through the DBR layers, it is partially reflected and transmitted at each interface. Because each layer has an optical thickness of a quarter-wavelength, the phase accumulated by propagating one-way through a single layer is always $\pi/2$. Combined with the phase shifts that occur upon reflection, all partial reflections from the incident wave will be in phase. For example, the first partial reflection ($E_{r,1}$) reflects at the $n_{\text{in}} \rightarrow n_2$ interface (lower to higher index), resulting in a π phase shift. The second reflection ($E_{r,2}$) accumulates a phase of π from propagation back and forth over the first layer, and experiences a 0 phase shift reflecting at the $n_2 \rightarrow n_1$ interface (higher to lower index), resulting in a total phase of π. The third reflection ($E_{r,3}$) accumulates π from propagating through two layers and experiences a π phase shift at the $n_1 \rightarrow n_2$ interface (lower to higher index), followed by another phase shift of π from propagating back through the two DBR layers. This results in a total phase of 3π for the third partial reflection. Continuing this exercise reveals that all partial reflections accumulate an odd multiple of π (e.g., $\pi, \pi, 3\pi, 5\pi$), causing them to interfere constructively (ΣE_r) and yielding the large reflectance of the DBR. The reflectance of a DBR can be analytically determined using, for example, the transfer matrix method (TMM) [92], where the peak reflectance of a DBR starting with a high-index layer and containing N pairs of high- and low-index layers is given as

$$R_{\text{DBR}} = \left[\frac{n_{\text{in}} - n_{\text{out}} \left(\frac{n_2}{n_1} \right)^{2N}}{n_{\text{in}} + n_{\text{out}} \left(\frac{n_2}{n_1} \right)^{2N}} \right]^2 , \tag{2.6}$$

where n_{in} and n_{out} are the refractive indices of the incident and outgoing media, as shown in **Fig. 2.3**. From **Eq. 2.6**, the variables that can be adjusted to achieve a large reflectance are either the number of mirror pairs (N) or the refractive-index contrast between the two media ($\frac{n_2}{n_1}$).

An advantage of forming the VCSEL cavity with DBRs is that the entire laser can be epitaxially grown in one step in a lattice-matched material system. By tuning the stoichiometric ratios of the semiconductor crystal, the refractive index of the layers can be precisely controlled during

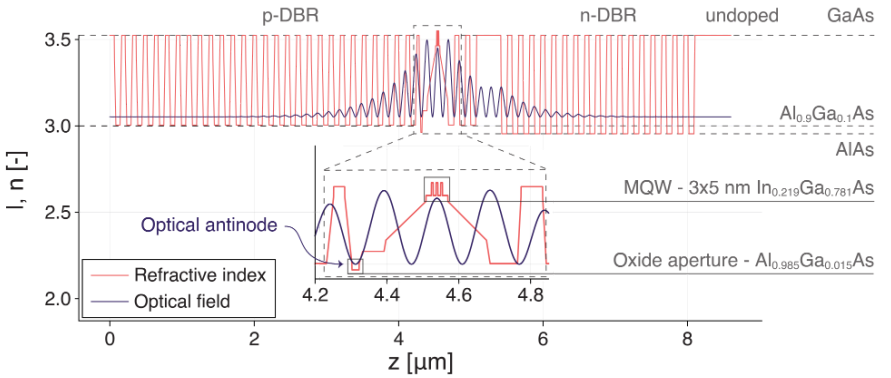

Figure 2.4: The refractive index profile created by the AlGaAs DBRs and the gain medium, together with the resulting intensity of the longitudinal optical standing wave in the fabricated VCSELs. The top-DBR consists of 28 mirror pairs alternating between GaAs/$Al_{0.9}Ga_{0.1}As$, and the bottom-DBR of 22 pairs of 3 GaAs/$Al_{0.9}Ga_{0.1}As$ + 19 GaAs/AlAs. The top and bottom DBRs are p- and n-type doped with carbon and silicon, respectively.

epitaxial growth. This allows DBR layers with alternating refractive indices to be grown with high precision and very smooth interfaces. This is one reason for the popularity of infrared GaAs-VCSELs. Because GaAs and aluminum arsenide (AlAs) have nearly the same lattice constant, a GaAs/AlAs DBR can satisfy both criteria for a high-reflectance mirror (**Eq. 2.6**): a large number of mirror pairs (N) can be grown with a relatively high index contrast ($\frac{n_2}{n_1}$) without generating defects or cracks. In addition, an epitaxially grown DBR can be doped, enabling the fabrication of electrical contacts directly on the mirror surfaces for current injection. An alternative mirror capable of achieving $R > 99\%$ is the subwavelength high-contrast grating, which offers significant advantages such as extreme compactness and polarization control [93, 94]. However, epitaxial DBRs remain the most common solution for forming the VCSEL cavity due to their straightforward fabrication process.

2.2.3 Longitudinal modes

The longitudinal cavity of the VCSEL is defined by the *pin* heterostructure and the DBRs, which confine both the charge carriers and photons in the longitudinal direction (z). **Figure 2.4** depicts the refractive index profile of the epitaxial material, overlaid with the simulated longitudinal optical field intensity for the fabricated GaAs-VCSELs. To

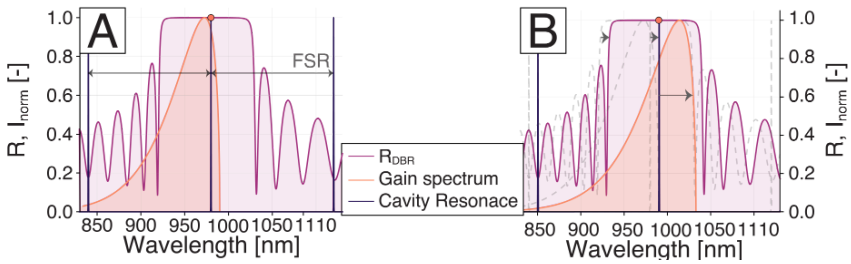

Figure 2.5: A) The gain spectrum of the MQW, the stopband DBR, and the longitudinal resonant wavelength of the VCSEL cavity, all three of which must be spectrally aligned to achieve lasing with the VCSEL. **B)** As the VCSEL is biased at a higher current, heat builds up in the cavity, which red-shifts the gain spectrum, the DBR stopband, and the longitudinal resonances.

achieve lasing, the gain spectrum of the MQWs, the stopband of the DBR, and the longitudinal cavity resonance must be spectrally aligned, as illustrated in **Fig. 2.5A**, where the longitudinal cavity resonance determines the lasing wavelength. As the VCSEL is operated (biased for electrical injection), thermal buildup inside the cavity induces a spectral redshift across all three spectra, as illustrated in **Fig. 2.5B**. The gain spectrum redshifts because GaAs, like semiconductors in general, has a temperature-dependent bandgap shrinkage (described by Varshni's relation). The bandgap reduction is primarily caused by an increase in the kinetic energy of the lattice, which intensifies electron-phonon interactions [95]. Simultaneously, the rising temperature also redshifts the DBR stopband and the longitudinal resonance. Aluminum gallium arsenide (AlGaAs) has a positive thermo-optic coefficient ($dn/dT > 0$) [96], which causes the DBR spectrum and the resonance to also redshift with temperature. However, the redshifts typically occur at different rates, where the gain spectrum shifts faster (≈ 0.3 nm/°C) than the cavity resonance (≈ 0.07 nm/°C) [97]. As the temperature continues to rise, the gain spectrum eventually sweeps past and spectrally outruns the cavity resonance. The increasing spectral mismatch, combined with carrier leakage and non-radiative Auger recombination, causes the gain to saturate and the VCSEL to stop increasing in output power, a phenomenon known as thermal rollover.

To counteract the thermal shifts, VCSELs can be designed with an

initial spectral offset, called detuning [86]. By deliberately blue-shifting the gain-spectrum peak relative to the cavity resonance at room temperature, the resonance aligns with the gain peak at an elevated internal temperature. This intentional offset delays the point at which the gain spectrum outruns the resonance, thereby increasing the maximum achievable output power before thermal rollover occurs. While measuring the gain spectrum is theoretically possible [98], it is very difficult for VCSELs. Instead, achieving an optimal detuning relies on photoluminescence or electroluminescence measurements combined with empirical experience. Beyond achieving an optimal output power, the detuning is a critical parameter for the high-speed dynamic performance of the VCSEL [5, 99].

Additionally, the length of the longitudinal cavity determines the free spectral range (FSR), which is the wavelength separation between adjacent longitudinal modes, shown in **Fig. 2.5**. The separation can be obtained from the derivative of the phase condition (**Eq. 2.4**) with respect to the mode number as

$$\Delta\lambda = \frac{\lambda^2}{2Ln_{\mathrm{g,eff}}}, \tag{2.7}$$

where L is the effective physical length of the cavity and $n_{\mathrm{g,eff}} = n_{\mathrm{eff}} - \lambda\frac{dn_{\mathrm{eff}}}{d\lambda}$ is the effective group index of the mode. For the fabricated VCSELs, the epitaxial structure was grown to form a 1λ-long optical cavity designed to emit at $\lambda = 980$ nm. This yields a free spectral range of $\Delta\lambda \approx 140$ nm, which is significantly wider than the gain spectrum of the InGaAs-MQWs (30–50 nm). Thus, only one longitudinal mode can be within the gain spectrum, ensuring that the fabricated VCSELs lase in a single longitudinal mode.

2.2.4 Oxide aperture

Beyond the longitudinal confinement, both charge carriers and photons must also be confined in the transverse direction [100]. The most common solution in modern GaAs VCSELs is to use an oxide aperture [101], achieved by incorporating one or more layers with a significantly higher aluminum content in the VCSEL DBRs [102, 103]. During fabrication, these epitaxial layers can be oxidized, and because the oxidation rate strongly depends on the aluminum content of the AlGaAs layers, it

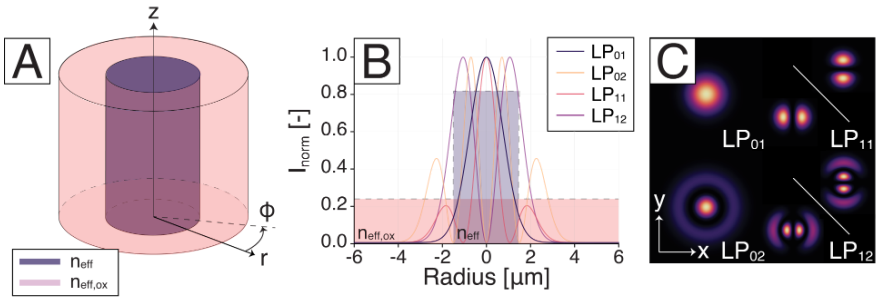

Figure 2.6: A) The effective step-index profile of the oxide-confined VCSEL. Because the formed oxide has a lower refractive index, the cladding region ($n_{\text{eff,ox}}$) has a lower refractive index than the core (n_{eff}), forming a waveguide. **B)** The radial intensity profiles of the first four LP modes of the VCSEL and the respective effective refractive index profiles (n_{eff} and $n_{\text{eff,ox}}$). **C)** The transverse distribution of the same four LP modes.

is possible to selectively oxidize the aluminum-rich layers [104]. The resulting oxide aperture simultaneously (and elegantly) solves both electrical and optical confinement. The formed oxide has higher electrical resistance and a lower refractive index ($n_{\text{ox}} = 1.5$–1.6 [105, 106]). The increase in electrical resistance funnels carriers into the central active region, while the lower refractive index creates a step-index waveguide for photon confinement [107].

The diameter of the oxide aperture, d_{ox}, is arguably the most critical parameter to control for an oxide-confined VCSEL, as it highly influences both the optical and electrical laser performance. Electronically, the oxide aperture defines the volume of the gain medium that must be pumped to population inversion. While a smaller aperture reduces the required volume and lowers the threshold current, it also reduces the cross-sectional area for the flux of charged carriers, thus increasing the electrical resistance of the VCSEL. This means that a smaller-aperture VCSEL has a lower threshold current but also reaches thermal rollover at a lower current due to larger heat buildup, limiting the maximum optical output power. Optically, the oxide aperture sets the transverse mode distribution of the VCSEL since it forms a waveguide by lowering the refractive index of the high-aluminum layer, as illustrated in **Fig. 2.6A**. The formed waveguide is commonly analyzed using the effective index method [108, 109]. In this method, the unoxidized core and the oxidized cladding are assigned effective refractive indices (n_{eff} and $n_{\text{eff,ox}}$)

weighted by the longitudinal electric field distribution in each region. Because the oxide forms radially inwards, the waveguide can be modeled as a cylindrical step-index fiber. Solving Maxwell's equations for this cylindrical geometry yields a set of exact vector modes, which are typically approximated as weakly guided linearly polarized (LP) modes [92]. The transverse intensity profile of these LP modes can be expressed as

$$I_{LP}(r,\phi) \propto |E_{LP}(r,\phi)|^2 = \left(\frac{2r^2}{\omega_0}\right)^2 \left[L_{p-1}^{(l)}\left(\frac{2r^2}{\omega_0}\right)\right] \begin{Bmatrix}\cos^2(l\phi)\\ \sin^2(l\phi)\end{Bmatrix} e^{-\frac{2r^2}{\omega_0}}, \tag{2.8}$$

where ω_0 is the $1/e^2$ beam waist radius of the fundamental mode, $L_{p-1}^{(l)}$ is the lth generalized Laguerre polynomial of order $p-1$, ϕ is the azimuthal angle, and r is the radius. For $l > 0$, the sin and cos factors represent two orthogonal states rotated by $90°/l$ with respect to each other. The radial distribution of the first four modes is shown in **Fig. 2.6B** together with the radial refractive index profile, while their transverse distributions are illustrated in **Fig. 2.6C**. As seen in **Fig. 2.6C**, the two indices (l and p) define the number of antinodes in the respective directions. p corresponds to the number of radial antinodes, whereas there are $2l$ azimuthal antinodes. The fundamental LP_{01} mode has the longest resonant wavelength (λ_{01}), and the wavelengths of the higher-order transverse modes are progressively shorter as

$$\lambda_{LP} = \lambda_{01}\left[1 - (2p + l - 1)\sqrt{\frac{\Delta n_{\mathrm{eff}}}{2\pi}}\frac{\lambda}{n_{\mathrm{eff}} d_{\mathrm{ox}}}\right]. \tag{2.9}$$

The diameter of the core region (d_{ox}) sets the radial extent of the waveguide, which in turn determines the transverse modes the step-index waveguide supports [86]. With a sufficiently small aperture, only the fundamental mode (LP_{01}) is guided and will experience a loss small enough to reach the lasing threshold (g_{th}). However, when the VCSEL is biased, light is always generated across the entire gain spectrum of the MQWs, creating a bias-dependent spectral background that is amplified and filtered by the cavity. The VCSEL is typically classified as a single-mode device when the emission from the fundamental mode is significantly stronger than any other amplified or lasing mode, as measured by the side-mode suppression ratio (SMSR). A VCSEL is considered single-mode if the SMSR exceeds 30 dB[5].

[5]Or, in plain words, when the fundamental mode emits an intensity 1000 times higher than any lasing or amplified mode.

Therefore, to achieve a single-mode VCSEL, the aperture must be small enough that only the fundamental mode (LP_{01}) is guided. However, as discussed earlier, a small aperture increases electrical resistance and limits maximum output power. The fabricated VCSELs utilize a single oxide layer centered on an optical *node* of the standing-wave field, as shown in **Fig. 2.4**. Positioning the aperture at the node minimizes modal overlap with the oxide layer, yielding the smallest possible effective refractive index step (Δn_{eff}) between the core and cladding regions of the VCSEL waveguide, a configuration referred to as a weakly guided VCSEL. As an example, the fabricated VCSEL has an effective index step of $\Delta n_{\text{eff}} = 0.000351$. The small index step allows for the largest possible waveguide that guides only the fundamental mode, which in turn yields the lowest electric resistance and the highest output power under single-mode operation.

2.2.5 Polarization state

The step-index model gives the transverse intensity distribution of the transverse modes (**Eq. 2.8**). However, since the electric field is vectorial, each transverse mode also has a certain linear polarization state in the plane of the epitaxial layer. Any polarization state can be described as a linear combination of two orthogonal states oriented with the major crystal axis of the semiconductor material. For the GaAs-VCSEL, the crystal has a zincblende lattice, which is optically isotropic, meaning the two orthogonal linearly polarized states for any transverse mode are degenerate and ideally share the same resonant wavelength. Furthermore, with a rotationally symmetric oxide aperture, the optical cavity has no in-plane asymmetry. Thus, a GaAs-VCSEL with a cylindrical cavity does not impose any preferential in-plane orientation for the electric field [110].

However, in fabricated devices, the ideal rotational symmetry is inevitably broken [27]. Defects from epitaxial growth and mechanical stress induced during fabrication can create a weak anisotropy, and the strong electric field of the *pin* junction contributes to a weak elasto-optic effect [111][6]. This results in a total weak in-plane birefringence, which typically aligns the emission with either of the two orthogonal major

[6]This is a very unfortunate citation numbering as it is easily confused for the crystallographic directions.

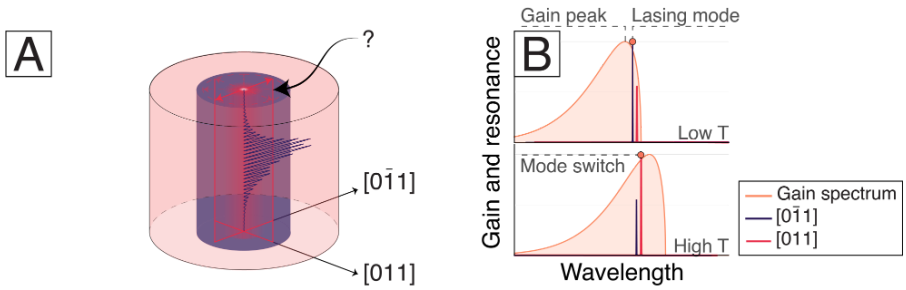

Figure 2.7: A) In a rotationally symmetric VCSEL cavity, the field of the lasing mode typically aligns with either the [011] or [0$\bar{1}$1] crystallographic axis of AlGaAs due to a weak anisotropy. **B)** As current increases in the VCSEL, the gain spectrum and resonance peaks shift in wavelength due to thermal build-up. Because unintentional anisotropy splits the two orthogonal polarization states in wavelength, the state can switch places relative to the gain-spectrum peak as the temperature (T) increases during operation.

crystallographic axes (the [011] or [0$\bar{1}$1] directions for GaAs grown on the (100) plane), as shown in **Fig. 2.7A**. Furthermore, the in-plane birefringence splits the resonant wavelengths of the two orthogonal modes (typically by a few tens of GHz [112]). Despite this built-in asymmetry, the unintentional birefringence is usually insufficient to pin the polarization to a single state across the full operating range of the VCSEL. One mechanism for the polarization instability is illustrated in **Fig. 2.7B**, where the lasing switches to the polarization state with the longer resonant wavelength as the bias current increases. For a VCSEL with a blue-detuned cavity at room temperature, the polarization mode with the slightly shorter wavelength is initially closer to the gain-spectrum peak. At threshold current, this mode experiences greater amplification and begins to lase first, suppressing the orthogonal mode by consuming available carriers. As the bias current increases, however, thermal buildup redshifts both the gain spectrum and the cavity resonances, as discussed earlier and shown in **Fig. 2.5B**. When the gain spectrum outruns the resonance, the modes will switch places relative to the peak of the gain spectrum. As the orthogonal state with the longer wavelength now experiences greater amplification from the gain medium, it can cause the VCSEL to switch polarization states.

Figures 2.8A-B present the typical polarization trends observed for the fabricated VCSELs with a standard, rotationally symmetric oxide

aperture. The typical trend for a single-mode VCSEL with a smaller oxide aperture ($d_{\mathrm{ox}} = 2\,\mu\mathrm{m}$) is presented in **Fig. 2.8A**, where the polarization state is initially aligned with the $[0\bar{1}1]$-axis near threshold due to the unintentional anisotropy. At bias currents exceeding $I_{\mathrm{b}} = 2$ mA, the measured polarization state appears to tilt away from this major crystallographic axis, as the optical power is now distributed between both axes. Since these devices operate in a single transverse mode, the measured tilt of the polarization plane is attributed to the lasing mode rapidly switching back and forth between the two orthogonal polarization states. This suggests that the cavity is bistable, where the mode-hopping is caused by stochastic spontaneous emission coupling into the lasing modes [113, 114]. The dwell times during such mode hopping in either of the orthogonal states have been measured to range from nanoseconds to seconds in air-post and proton-implanted VCSELs [115, 116]. Since the polarization-resolved current-power (PIP) measurements in **Fig. 2.8A-B** are acquired with a relatively long integration time (1.6 s), the measurements are believed to be averaged over many dwell times. As a result, the measured tilt of the polarization plane means that the lasing has a longer dwell time in the state aligned with the $[0\bar{1}1]$ axis. In **Fig. 2.8B**, the typical trend for a larger aperture ($d_{\mathrm{ox}} = 3\,\mu\mathrm{m}$) single-mode VCSEL is presented, where the device again lases preferentially along the $[0\bar{1}1]$ axis near threshold, but eventually undergoes a distinct polarization switch to the orthogonal state at around $I_{\mathrm{b}} = 2$–4 mA. At larger bias currents, the VCSEL goes into the same mode-hopping behavior as the smaller aperture device.

In several applications, it is desirable to have a VCSEL with a well-defined polarization state, with as much optical power as possible[7]. It is possible to modify the VCSEL cavity to pin the polarization, i.e., forcing the laser to emit light in a single polarization state. The idea of pinning the polarization is to introduce anisotropy to the VCSEL cavity to separate the two orthogonal states in wavelength or differentiate the gain/loss for each state. One modification to pin the polarization state of the VCSEL is to etch a subwavelength surface grating, a common option because of its compatible fabrication process and relatively high performance [117, 118]. The grating creates an anisotropic effective permittivity in the DBR, which is different for an electric field that is

[7] Especially for metasurface integration, since they are, in most cases, polarization-sensitive, as we will see in the next chapter.

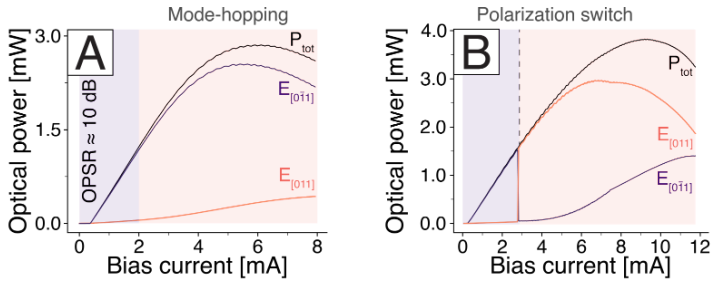

Figure 2.8: A) Polarization-resolved current-power (PIP) measurement for a bottom-emitting VCSEL with a 2 µm diameter oxide aperture. Near threshold, the VCSELs lase with the field aligned with the $[0\bar{1}1]$-axis. At larger bias currents ($I_b > 2$ mA), the lasing state is driven into an unpredictable mode-hopping state. **B)** Similarly, VCSELs with a 3 µm diameter oxide aperture mainly lase with the field aligned with the $[0\bar{1}1]$-axis near threshold. However, as the bias increases, the polarization clearly switches to the orthogonal [011]-state.

parallel ($\epsilon_{||}$) or perpendicular ($\epsilon_{\perp}$) to the lines of the grating [119]. In **Fig. 2.9A**, such a subwavelength grating is schematically shown. The effective anisotropic permittivity can be estimated by spatial averaging of the electric and displacement fields as

$$\begin{aligned} \epsilon_{||} &= d\epsilon_{\mathrm{g}} + (1-d)\epsilon_{\mathrm{f}}, \\ \epsilon_{\perp} &= \frac{\epsilon_g \epsilon_{\mathrm{f}}}{d\epsilon_{\mathrm{f}} + (1-d)\epsilon_{\mathrm{g}}}, \end{aligned} \tag{2.10}$$

where ϵ_{g} and ϵ_{f} are the permittivities of the grating and the material filling the grating grooves, respectively. $d = a/P$ is the duty cycle of the grating, defined here as the ridge-to-period ratio. In **Fig. 2.9B**, the anisotropic refractive index of the grating is shown for a GaAs grating filled with air ($n_{\mathrm{f}} = 1$) and with SiN_x ($n_{\mathrm{f}} = 1.99$)[8] as a function of the duty cycle. As shown, the duty cycle can tailor the refractive-index contrast between the orthogonal states. Furthermore, when the field is parallel to the grating lines, the effective refractive index is relatively high, closer to that of the grating medium. In the perpendicular case, it is lower, closer to the index of the material within the grating grooves. As a consequence, the refractive-index contrast between the two states is significantly reduced when the grating grooves are filled with a material

[8]The refractive index of SiN_x at the designed lasing wavelength of the fabricated VCSELs, $\lambda_0 = 980$ nm.

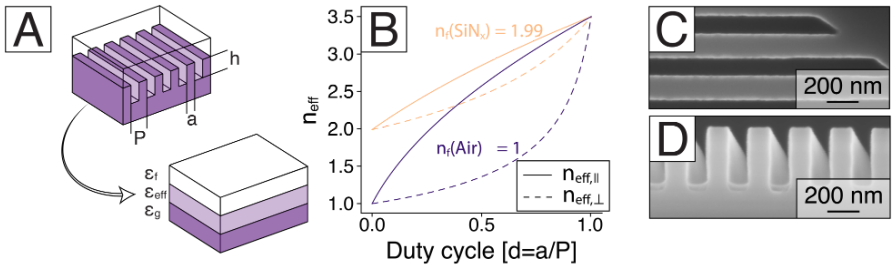

Figure 2.9: **A)** Schematic structure of the effective anisotropic permittivities of the subwavelength grating for polarization pinning. **B)** The anisotropic refractive index from **Eq. 2.10** as a function of the duty cycle of the grating ($d = a/P$). The lasing modes will experience different refractive indices depending on whether the electric field is parallel (filled lines) or perpendicular (dashed lines) to the grating lines. **C)** SEM image of the top view of an etched subwavelength grating in the top mirror of a bottom-emitting VCSEL. **D)** SEM image of a cross-section of an etch test for the subwavelength gratings.

that has a larger refractive index than air.

Without the grating, the DBR is designed to produce constructive interference from all the partial reflections at all the interfaces of the DBR, as illustrated in **Fig. 2.3**. The etched grating introduces new partial reflections that do not constructively interfere with the other reflections, thus reducing the total reflectance of the DBR. Since the new partial reflection from the grating depends on the refractive index of the grating, the anisotropic index means that the reflectance from the DBR will be altered depending on the direction of the electric field vector relative to the grating lines. This, in turn, means the two orthogonal states will have different gain thresholds (**Eq. 2.5**), which can suppress lasing in the state with the higher threshold gain. In **Fig. 2.9C**, a SEM image of the top view of such an etched subwavelength grating that pins the polarization in a bottom-emitting VCSEL is shown. Lastly, **Fig. 2.9D** shows a cross-section of an etch test for the grating fabrication[9].

[9]Simulation, fabrication, and measurement data are found in the appended paper [120].

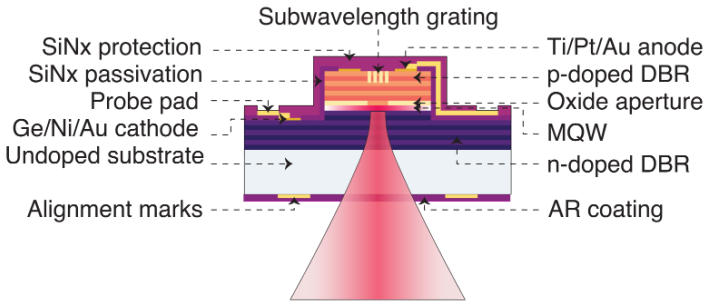

Figure 2.10: Schematic cross-section of the fabricated bottom-emitting VCSELs with integrated subwavelength grating for polarization pinning.

2.3 VCSEL fabrication

The epitaxially grown structures for the VCSELs were grown by Jenoptik using metal-organic chemical vapor deposition (MOCVD). In MOCVD, gaseous organic compounds transport the three materials (Al, Ga, In) into a reactor, where they react with gaseous AsH_3 and deposit onto a heated substrate. Doping of the *p*-type and *n*-type DBRs is achieved by introducing carbon and silicon, respectively, during the epitaxial growth. A cross-section of the fully processed VCSEL is illustrated in **Fig. 2.10**. The full process flow for the bottom-emitting VCSEL is presented in **Fig. 2.11** together with a microscope image of the top view of a VCSEL before the final SiN_x protection layer. The fabrication process is summarized as:

1. **Wafer preparation:** Patterning of alignment marks on both sides of the wafer for alignment between the VCSEL and metasurface. The alignment marks are deposited on the full wafer since the laser writer used can only perform backside alignment for larger samples[10]. The resulting alignment between the backside and the VCSEL is ±1 µm, measured from the center of the emitted beam to the alignment marks on the substrate side. The marks consist of an evaporated 20/50/100 nm Ti/Pt/Au stack. The Pt layer is crucial to prevent diffusion between Au and Ti, which otherwise degrades the reflectivity of the alignment marks during subsequent thermal processing. The substrate side is protected with a 400 nm

[10]For this project, the addition of said laser writer in 2022 to our cleanroom was a large upgrade, for both the precision and the ease of the backside alignment process.

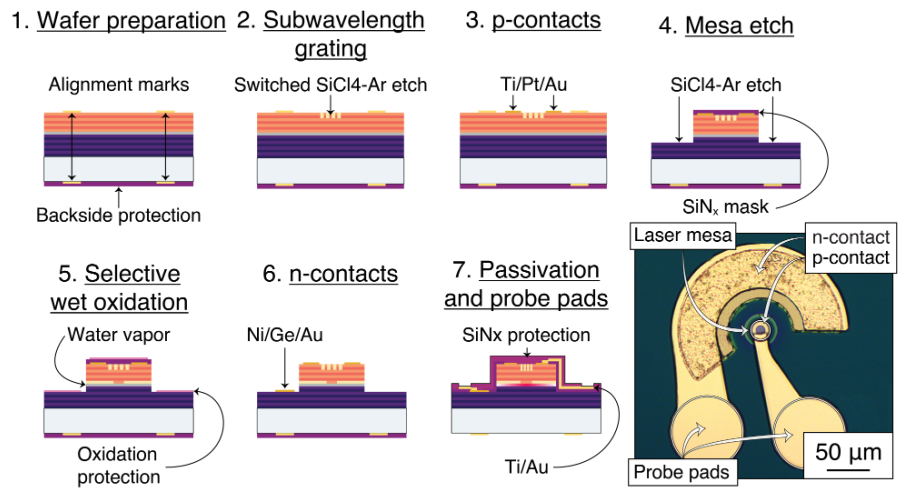

Figure 2.11: Process flow for the bottom-emitting VCSELs together with a microscope image of the top view of a fabricated VCSEL during the final step (step 7) before the deposition of the final protective SiN_x layer.

SiN_x film, and the wafer is cleaved into 0.8×1.0 cm^2 pieces for further processing.

2. **Subwavelength Grating:** Etching of the subwavelength grating to pin the polarization state. The grating is fabricated by sputtering a 100-nm-thick SiO_2 film and patterning it with AR-P 6200 resist by EBL. The grating pattern is then transferred into the SiO_2 with a CF_4-O_2 reactive ion etch (RIE), followed by etching the grating into the AlGaAs layers of the DBR with a switched Ar-$SiCl_4$ and O_2 reactive ion etch[11] using an inductively coupled plasma reactive ion etch (RIE-ICP).

3. **p-contacts:** Patterning of the metal contact for current injection on the *p*-side. The p-contact consists of the same evaporated 20/50/100 nm Ti/Pt/Au stack as the alignment marks. Because the top GaAs layer is heavily carbon-doped ($5 \cdot 10^{19}$ cm^{-3}), this stack forms a low-resistance ohmic contact without requiring thermal annealing. After the deposition, the contact quality is verified using the transfer length method (TLM).

[11] More details of the switched GaAs etching process are in the next chapter on metasurfaces.

4. **Mesa etch:** The VCSEL mesa is etched to expose the bottom *n*-doped DBR for contact deposition. The AlGaAs etching is performed with a sputtered 350 nm SiN_x film as a hard mask for an $Ar/SiCl_4$ ICP-RIE etch.

5. **Selective wet oxidation:** To protect the chip from oxidation, a SiN_x protective layer is deposited and etched away only at the sidewalls of the VCSEL mesa. The selective oxidation is performed in a furnace at 410°C using water vapor at a pressure of ≈ 0.5 bar. The targeted aperture diameter is $d_{ox} = 2$–3 µm, for single-mode operation. Dedicated witness mesas, mesas without patterned p-contacts, are then etched to measure the achieved aperture diameters across the chip. **Figure 2.12A** presents a microscope image of the exposed oxide aperture of an etched witness mesa, while **Fig. 2.12B** presents the oxidation rate at 410°C. The radial oxidation rate at 410°C is typically 0.24 µm/min, with a spread of ±4 % across the fabricated chips when targeting a single-mode aperture. The black dots in **Fig. 2.12C** mark the positions of the witness mesas across a 0.8×1.0 cm^2 chip, with linear interpolation to show the oxidation-rate gradient. Because of this oxidation rate gradient, it is difficult to achieve the exact same aperture size for every VCSEL. However, the lithographically defined mesa diameters are intentionally varied to counteract the oxidation-rate gradient to achieve a more uniform aperture distribution.

6. **n-contacts:** Patterning of the metal contact for current injection on the *n*-side. The contacts consist of an evaporated 20/52/100 nm Ni/Ge/Au stack. Because the n-type GaAs layer cannot be as heavily silicon-doped ($1 \cdot 10^{18}$ cm^{-3}) as the p-side can be carbon-doped, the contact is thermally annealed at 390°C. This drives Ge diffusion from the metal into the GaAs, heavily doping the semiconductor interface to create an ohmic contact. After annealing, the n-contact quality is verified using TLM.

7. **Passivation and probe pads:** The entire chip is passivated with a sputtered 300-nm-thick SiN_x film. The film is etched to access the contacts, followed by a lift-off of sputtered 50/450 nm Ti/Au pads for probing or wirebonding the VCSELs. Afterward, the VCSEL side is protected for the subsequent metasurface fabrication by an additional 300 nm SiN_x layer, which is etched open only to access the probe pads. The probe pads are additionally reinforced by a

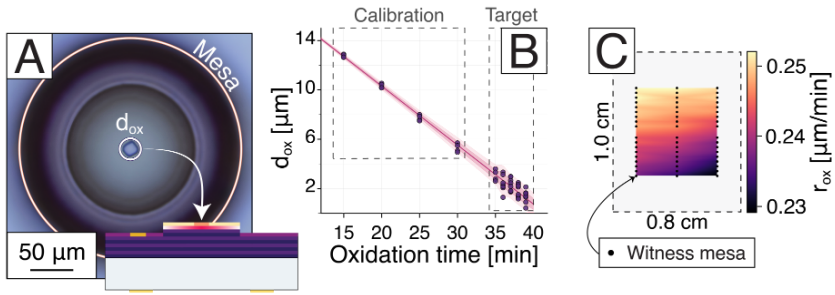

Figure 2.12: **A)** Microscope image of an etch witness mesa with the oxide aperture exposed (d_{ox}). **B)** Resulting oxide aperture diameters as a function of the oxidation time at 410°C. **C)** The oxidation rate gradient over the fabricated chips when selectively wet oxidized for 39 min. The dashed outline marks the outline of the 0.8×1.0 cm^2 chip, and the black dots mark the positions of the witness mesas. The gradient is linearly interpolated between the measured oxide diameters (d_{ox}) of the witness mesas.

lift-off process of yet another sputtered stack of 50/450 nm Ti/Au, and the protective SiN_x film on the metasurface side is removed. For devices tested without metasurfaces, a SiN_x layer is deposited on the substrate side to serve as an anti-reflection (AR) coating, reducing back reflections from the GaAs-to-air interface.

2.4 Static VCSEL characterization

Because our metasurface integration focuses on shaping the wavefront of the beam emitted from the VCSEL rather than high-speed modulation, this characterization covers the static performance of the fabricated lasers. We characterize the VCSELs by measuring their current-power-voltage (IPV), polarization-resolved current-power (PIP), spectral, and far-field beam characteristics.

Current-power-voltage (IPV)

The basic characterization of a VCSEL is the measurement of optical output power and voltage as a function of the bias current (IPV), as shown in **Fig. 2.13A**. The five key parameters that can be extracted from the IPV curve are: the threshold current (I_{th}), the turn-on voltage (V_{on}), the slope efficiency $\left(\frac{dP_{opt}}{dI_b}\right)$, the differential resistance, $\left(\frac{dV_b}{dI_b}\right)$, and

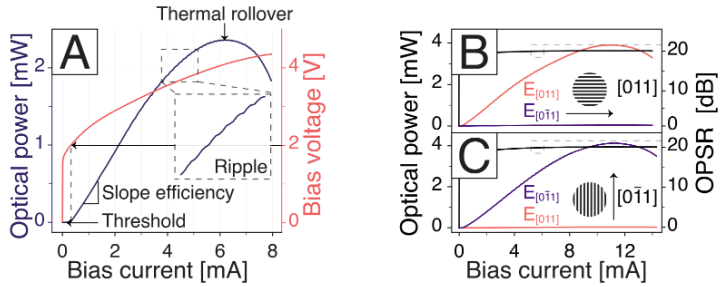

Figure 2.13: A) Current-power-voltage (IPV) characteristics of the fabricated VCSELs with $d_{\mathrm{ox}} = 2\,\mu\mathrm{m}$. **B)** PIP measurements of the VCSEL with an integrated subwavelength grating when the grating lines are aligned with the [011]-axis. **C)** Similarly, the PIP measurements with the grating lines aligned with the [0$\bar{1}$1]-axis. The grating effectively pins the polarization state of the lasing mode to a field parallel to the grating lines. This results in a predictable polarization state of the emitted beam, with an OPSR = 20 dB over the entire biasing range.

the maximum output power at thermal rollover (P_{max}). Lasing initiates at the threshold current (I_{th}), the point at which the amplification of the optical mode surpasses the total cavity losses. The corresponding voltage to I_{th} is the turn-on voltage (V_{on}). Above threshold current, the optical power increases linearly, with a rate called the slope efficiency $\left(\frac{\mathrm{d}P_{\mathrm{opt}}}{\mathrm{d}I_{\mathrm{b}}}\right)$. Similarly, the differential resistance $\left(\frac{\mathrm{d}V_{\mathrm{b}}}{\mathrm{d}I_{\mathrm{b}}}\right)$ is extracted from the slope of the voltage-current curve and represents the dynamic electrical resistance of the VCSEL during operation. As discussed previously, increasing the bias current will increase thermal build-up, which increases spectral misalignment between the cavity resonance and the gain spectrum, thermally excites carriers out of the quantum wells, and increases Auger recombination. As a result, the VCSEL goes into thermal rollover and reaches its maximum output power, P_{max}. Furthermore, for the bottom-emitting VCSELs, the IPV curve exhibits a ripple caused by back-reflections from the GaAs-to-air substrate interface, as seen in the inset of **Fig. 2.13A**. To reduce this unwanted reflection, a $\lambda/4$ $\mathrm{SiN_x}$ AR coating is sputtered on the GaAs substrate of all VCSELs characterized without a metasurface. Accounting for fabrication tolerances, TMM calculations estimate a residual reflection of $\approx 3\%$ for the deposited AR coating.

Polarization-Resolved Current-Power (PIP)

The static polarization characteristics are evaluated similarly to the IPV, with the addition of a rotatable linear polarizer in the optical path. First, the total optical output power (P_{opt}) is recorded without the polarizer. Afterward, the polarizer is introduced and oriented to suppress emission aligned with the $[01\bar{1}]$ crystallographic axis, thereby isolating the power of the orthogonal state ($P_{[011]}$). Finally, the polarizer is rotated by 90° to suppress the [011] emission, capturing the power of the orthogonal mode ($P_{[0\bar{1}1]}$). The figure of merit for polarization pinning is called the orthogonal polarization suppression ratio (OPSR), defined as the logarithm of the power in the desired polarization state over the unwanted orthogonal state[12]. The PIP measurements are performed with a photodiode (PD) using an integration time of 1.6 s. In the previous section, **Fig. 2.8A-B** presents two such PIP measurements showing the unpredictable polarization state of the fabricated VCSELs without an integrated subwavelength grating. By integrating a subwavelength grating into the top mirror of the VCSEL, the polarization state is pinned to the polarization state with an electric field parallel to the grating lines, as shown in **Fig. 2.13B-C**, achieving an OPSR greater than 20 dB across the entire biasing range.

Spectrum

The VCSEL wavelength spectrum is captured by focusing the emission into a fiber connected to an optical spectrum analyzer (OSA). The spectrum of a single-mode VCSEL with an oxide aperture diameter of $d_{\text{ox}} = 2\ \mu\text{m}$ is presented in **Fig. 2.14A**. Beyond the primary lasing peak, the spectrum contains a broad spontaneous-emission background from the MQWs, along with amplified peaks corresponding to higher-order transverse cavity modes. The inset in **Fig. 2.14A** shows the change in the wavelength of the fundamental mode (LP_{01}) as a function of the bias current (I_{b}). The shift is red due to the positive thermo-optic coefficient. A VCSEL is classified as single-mode when the SMSR, the intensity difference between the fundamental mode and the strongest higher-order mode, exceeds 30 dB. As seen in **Fig. 2.14B**, the fabricated VCSELs are single-mode when the oxide aperture is smaller than 3.5 µm. This comparison is made at a bias current above the threshold for all the mea-

[12] $\text{OPSR} = \log_{10}\left(\frac{P_1}{P_2}\right)$, where P_1 is the desired polarization state and P_2 is the orthogonal state.

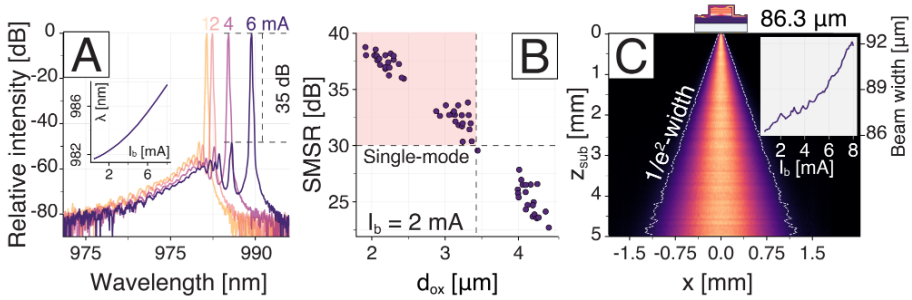

Figure 2.14: A) The spectra of the single-mode VCSEL with an oxide aperture diameter of $d_{\mathrm{ox}} = 2\,\mu\mathrm{m}$ for different bias currents. Inset: The red-shift of the fundamental (LP_{01}) mode as a function of the bias current. **B)** Measured SMSR as a function of the oxide aperture diameter (d_{ox}). The SMSR is compared at a bias current above the threshold for all aperture diameters ($I_{\mathrm{b}} = 2$ mA). **C)** Cross-section of the emitted far-field of the single-mode VCSEL ($d_{\mathrm{ox}} = 2\,\mu\mathrm{m}$) based on measurements and backpropagation of the electric field. Inset: The $1/e^2$-beam width at the substrate surface as a function of the bias current (I_{b}).

sured aperture diameters ($I_{\mathrm{b}} = 2$ mA). However, the SMSR degrades at higher bias currents, as uneven carrier consumption across the active region can amplify the higher-order transverse modes [86]. In addition, for larger bias currents ($I_{\mathrm{b}} = 6$ mA), the PIP measurements in **Fig. 2.8A-B** show emitted light associated with both orthogonal states, while the spectrum in **Fig. 2.14A** only shows a single lasing peak at the same current. This implies that unintentional built-in anisotropy splits the resonant wavelengths of the two orthogonal polarization states by less than the resolution limit of the OSA ($\Delta\lambda < 0.2$ nm).

Far-Field Emission

To design the metasurface, it is important to know the beam width of the emitted beam as it is incident on the substrate. To characterize this width, the far-field emission of the single-mode VCSEL is captured by imaging a diffuse plate at a distance (z_{sub}) from the substrate. Because the diffuse plate cannot be placed in direct contact with the substrate, the $1/e^2$-beam width is captured at several distances, as close as $z_{\mathrm{sub}} \approx 1.5$ mm, and then analytically back-propagated to the substrate plane. A cross-section of a measured z-stack, together with the analytically calculated cross-sections, is presented in **Fig. 2.14C** for a VCSEL with an

oxide aperture diameter of $d_{\mathrm{ox}} = 2\,\mu\mathrm{m}$. This yields a beam width of $w_0 = 86.3\,\mu\mathrm{m}$[13] at the GaAs substrate interface at $I_{\mathrm{b}} = 2$ mA. In addition, the beam width is not entirely constant under operation. Heating within the active region creates a radial thermal gradient that alters the refractive-index profile of the cavity. The gradient acts as a thermal lens, inducing additional focusing of the optical field and, in turn, increasing the far-field divergence of the emitted beam. The inset in **Fig. 2.14C** shows the increase in the beam width at the GaAs substrate as a function of the bias current for the $d_{\mathrm{ox}} = 2\,\mu\mathrm{m}$ device.

[13]The near-field of the beam is also captured in an inverted microscope in the fourth chapter, which is in good agreement with this methodology.